Supporting Information for:

Nickel(II) radical complexes of thiosemicarbazone ligands appended by salicylidene, aminophenol and aminothiophenol moieties.

Amélie Kochem, Gisèle Gellon, Olivier Jarjayes, Christian Philouze, Amaury du Moulinet d'Hardemare, Maurice van Gastel and Fabrice Thomas

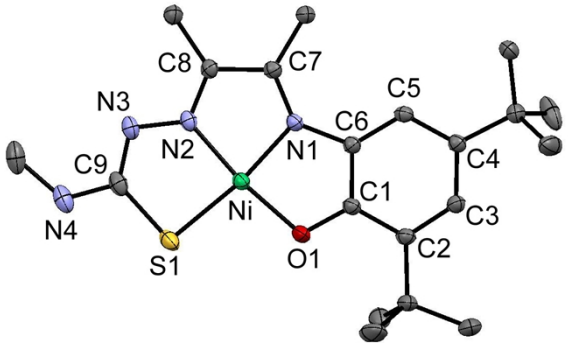

Table S1. Comparison of Experimental and Calculated Bond lengths (Angstroms) for 2, 2^+ and 2^-.

Bond	**2** (exp.)	**2** (calcd.)	$\mathbf{2}^+$ (calcd.)	$\mathbf{2}^-$ (calcd.)
C1-O1	1.338	1.325	1.314	1.332
C1-C2	1.422	1.429	1.434	1.421
C2-C3	1.390	1.395	1.389	1.406
C3-C4	1.416	1.416	1.426	1.406
C4-C5	1.393	1.390	1.394	1.402
C5-C6	1.407	1.410	1.404	1.408
C1-C6	1.424	1.434	1.451	1.438
N1-C6	1.426	1.397	1.383	1.393
N1-C7	1.307	1.323	1.337	1.362
C7-C8	1.488	1.459	1.441	1.420
N2-C8	1.313	1.327	1.349	1.356
N2-N3	1.384	1.355	1.328	1.368
N3-C9	1.323	1.333	1.351	1.316
C9-S1	1.760	1.758	1.755	1.759
Ni-O1	1.846(2)	1.877	1.849	1.884
Ni-N1	1.870(2)	1.864	1.865	1.860
Ni-N2	1.838(2)	1.847	1.836	1.829
Ni-S1	2.173(1)	2.184	2.166	2.201

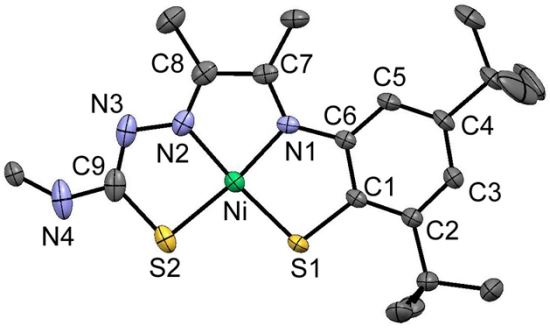

Table S2. Comparison of Experimental and Calculated Bond lengths (Angstroms) for 3, 3^+ and 3^-.

Bond	**3** (exp.)	**3** (calcd.)	$\mathbf{3}^+$ (calcd.)	$\mathbf{3}^-$ (calcd.)
C1-O1	1.773	1.783	1.752	1.779
C1-C2	1.412	1.421	1.429	1.420
C2-C3	1.379	1.406	1.397	1.409
C3-C4	1.385	1.403	1.414	1.403
C4-C5	1.385	1.395	1.393	1.397
C5-C6	1.392	1.404	1.404	1.411
C1-C6	1.417	1.419	1.434	1.432
N1-C6	1.425	1.417	1.400	1.394
N1-C7	1.320	1.326	1.337	1.370
C7-C8	1.467	1.456	1.447	1.417
N2-C8	1.295	1.328	1.338	1.351
N2-N3	1.376	1.349	1.331	1.366
N3-C9	1.321	1.338	1.346	1.318
C9-S1	1.761	1.754	1.765	1.758
Ni-S1	2.117	2.147	2.118	2.159
Ni-N1	1.880	1.882	1.886	1.882
Ni-N2	1.863	1.862	1.865	1.850
Ni-S1	2.160	2.183	2.155	2.195

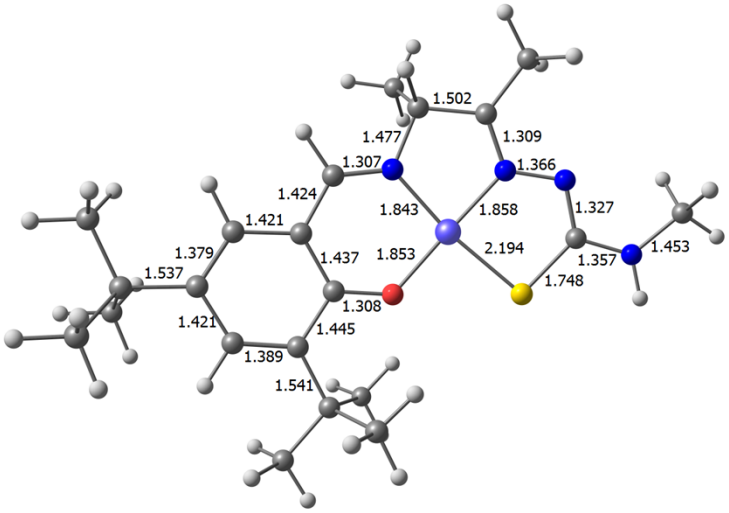

Figure S1. Geometry optimized structure of **1** and selected bond distances.

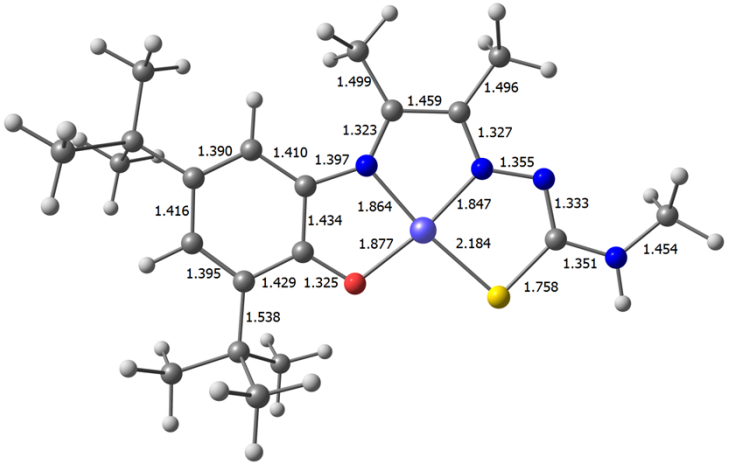

Figure S2. Geometry optimized structure of **2** and selected bond distances.

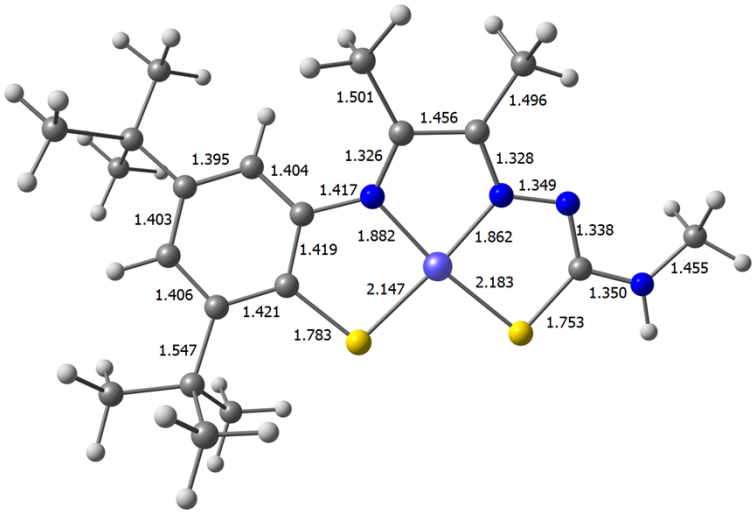

Figure S3. Geometry optimized structure of **3** and selected bond distances.

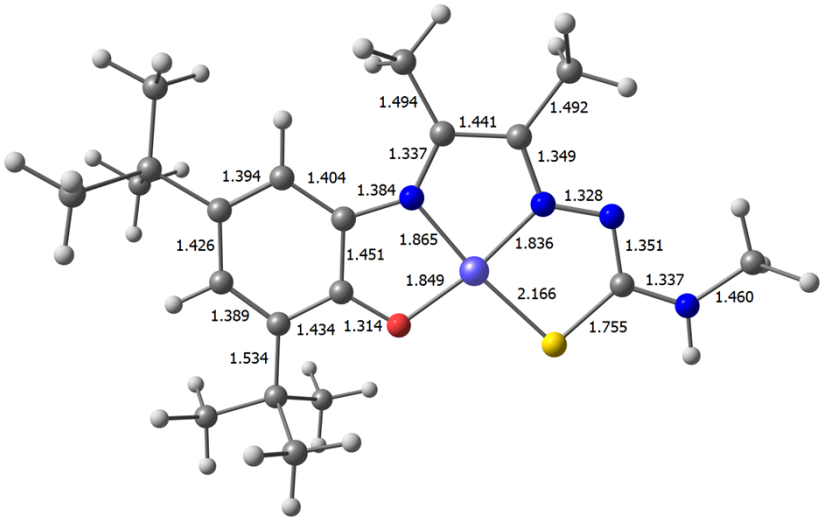

Figure S4. Geometry optimized structure of $\mathbf{2}^{+}$ and selected bond distances (doublet state).

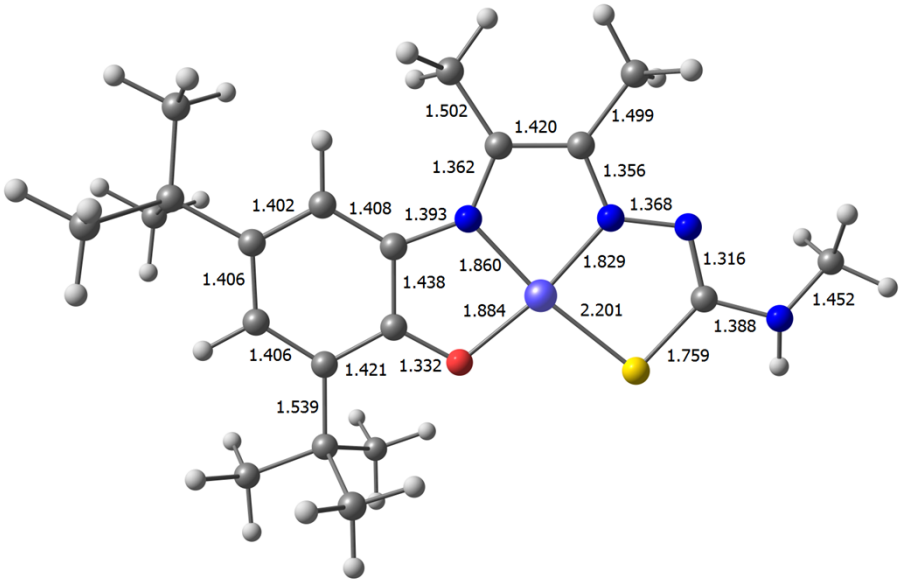

Figure S5. Geometry optimized structure of $\mathbf{2}^{-}$ and selected bond distances (doublet state).

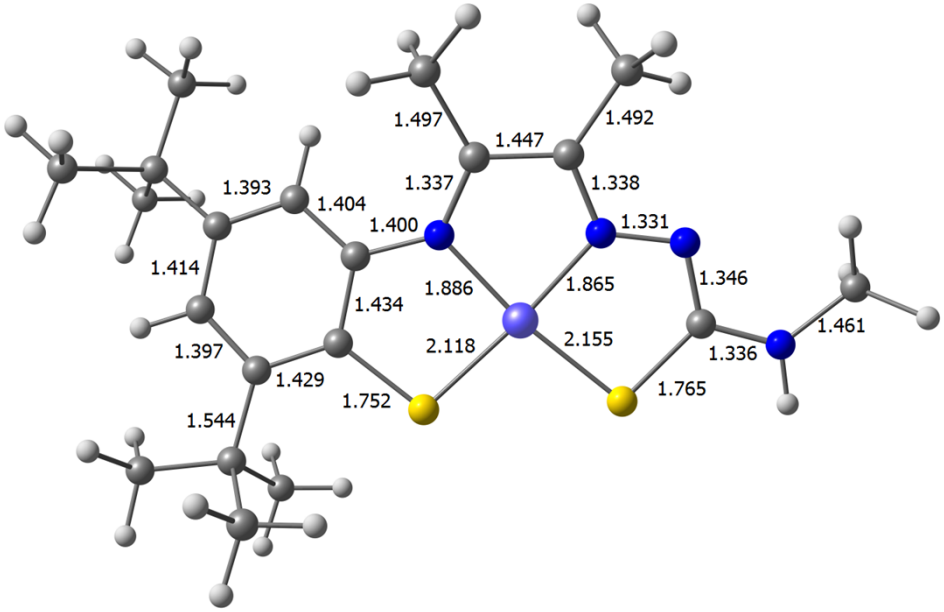

Figure S6. Geometry optimized structure of $\mathbf{3}^{+}$ and selected bond distances (doublet state).

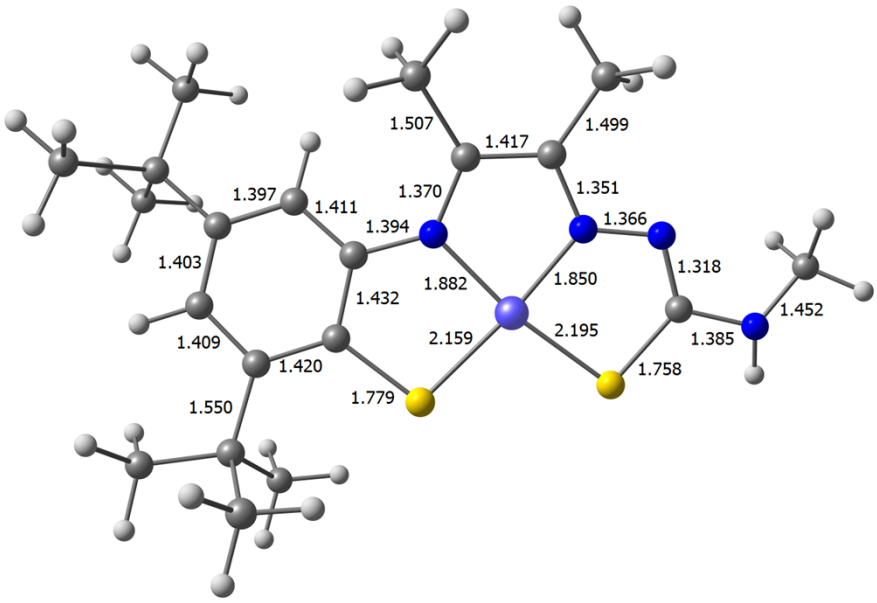

Figure S7. Geometry optimized structure of $\mathbf{3}^{-}$ and selected bond distances (doublet state).

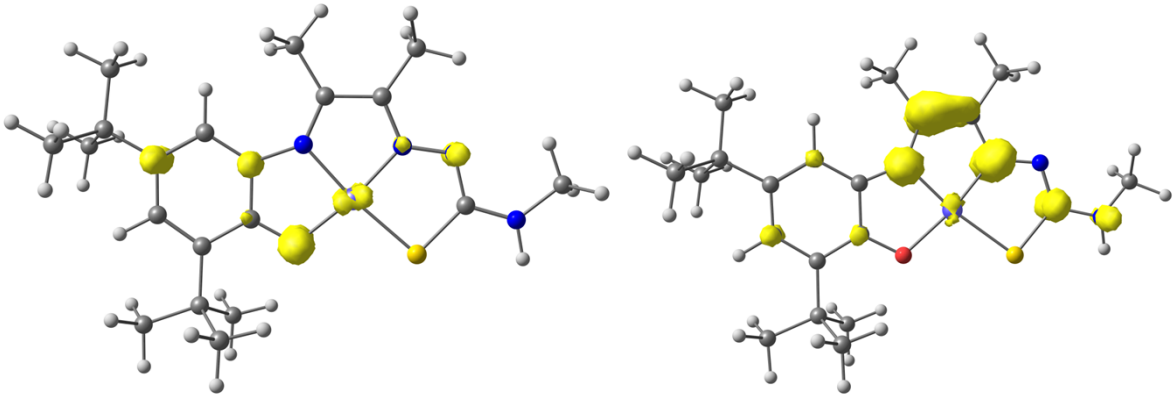

Figure S8. Spin density plots of a) $\mathbf{2}^{+}$ and b) $\mathbf{2}^{-}$(doublet state).

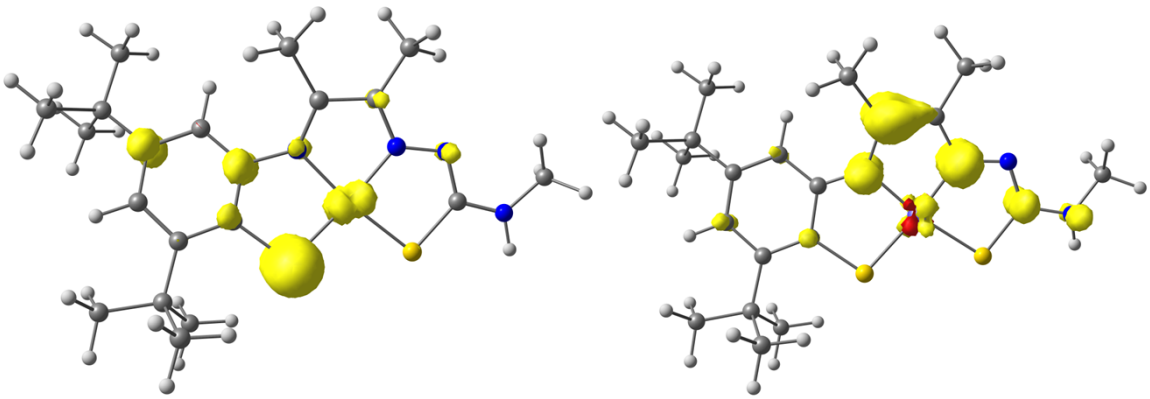

Figure S9. Spin density plots of a) $\mathbf{3}^{+}$ and b) $\mathbf{3}^{-}$(doublet states).

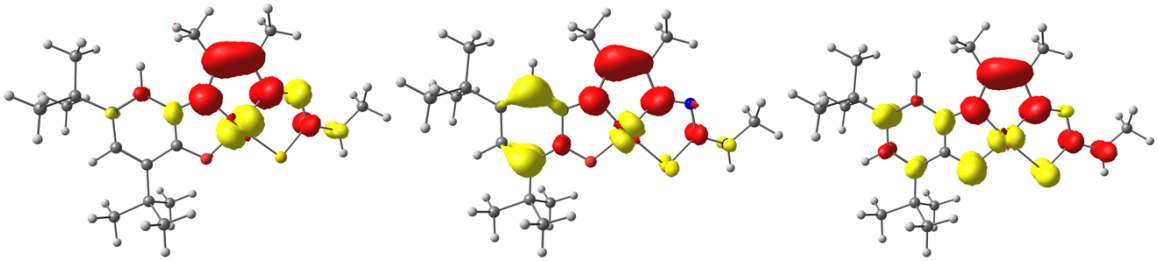

379 nm, *f* = 0.35 **402 nm *f* = 0.21** **820 nm, *f* = 0.06**

Figure S10. TD-DFT assignment of the electronic transitions of **2**. The diagrams give difference electron densities where red corresponds to positive density and yellow to negative density.

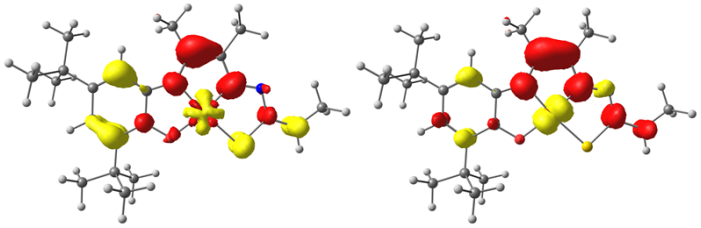

388 nm *f* = 0.57 **412 nm, *f* = 0.016**

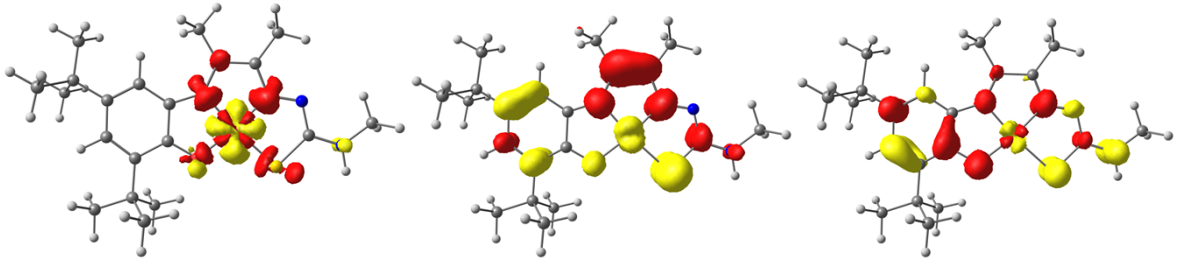

413 nm, *f* = 0.043 **530 nm *f* = 0.026** **568 nm, *f* = 0.046**

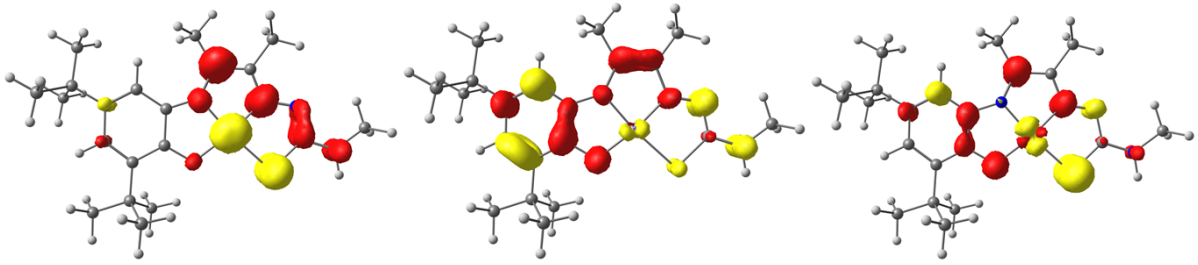

613 nm, *f* = 0.041 **792 nm *f* = 0.06** **1098 nm, *f* = 0.034**

Figure S11. TD-DFT assignment of the electronic transitions of $\mathbf{2}^{+}$. The diagrams give difference electron densities where red corresponds to positive density and yellow to negative density.

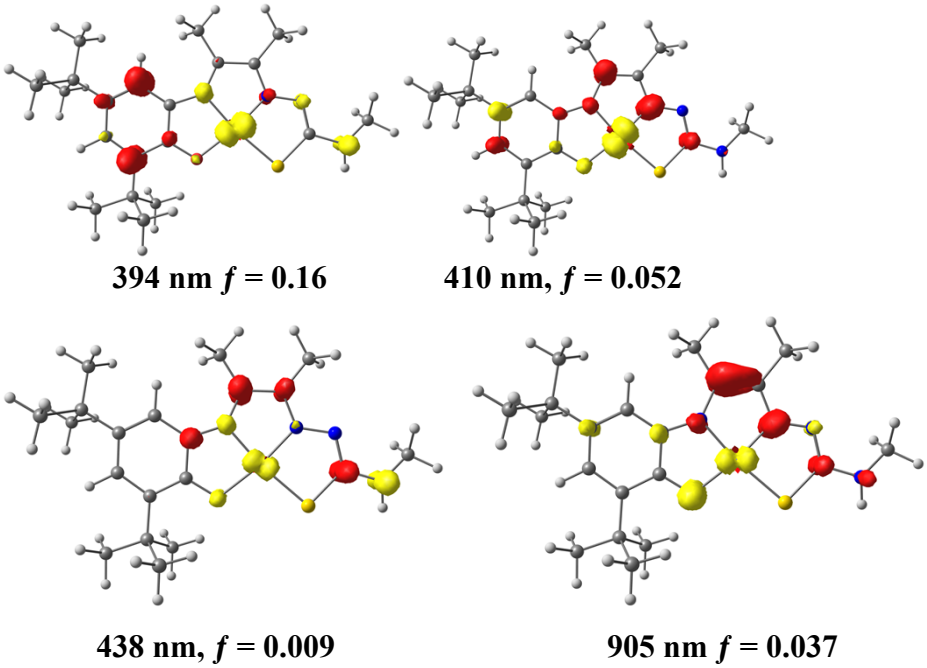

Figure S12. TD-DFT assignment of the electronic transitions of **2**$^{-}$. The diagrams give difference electron densities where red corresponds to positive density and yellow to negative density.

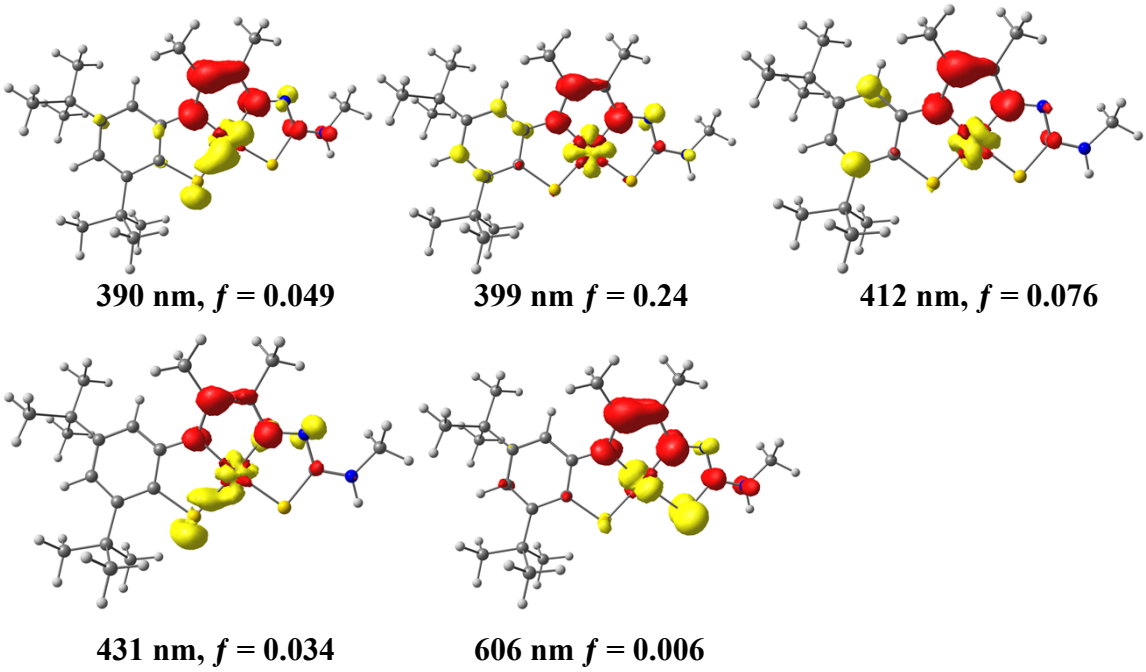

Figure S13. TD-DFT assignment of the electronic transitions of **3**. The diagrams give difference electron densities where red corresponds to positive density and yellow to negative density.

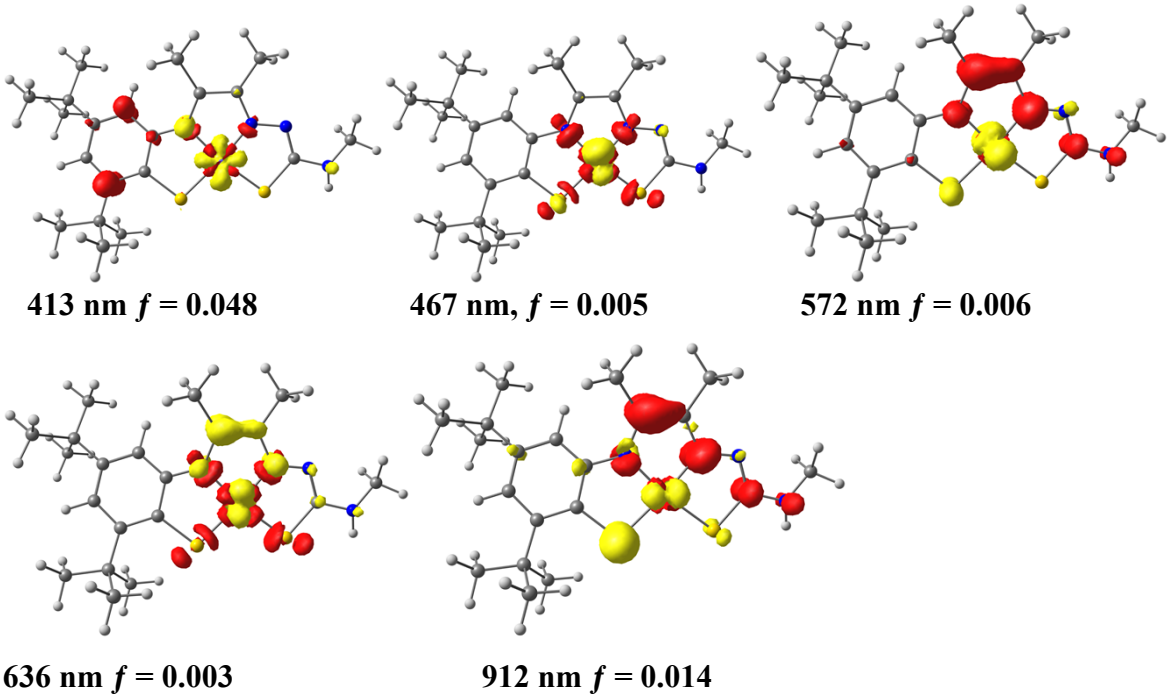

Figure S14. TD-DFT assignment of the electronic transitions of $\mathbf{3}^{-}$. The diagrams give difference electron densities where red corresponds to positive density and yellow to negative density.

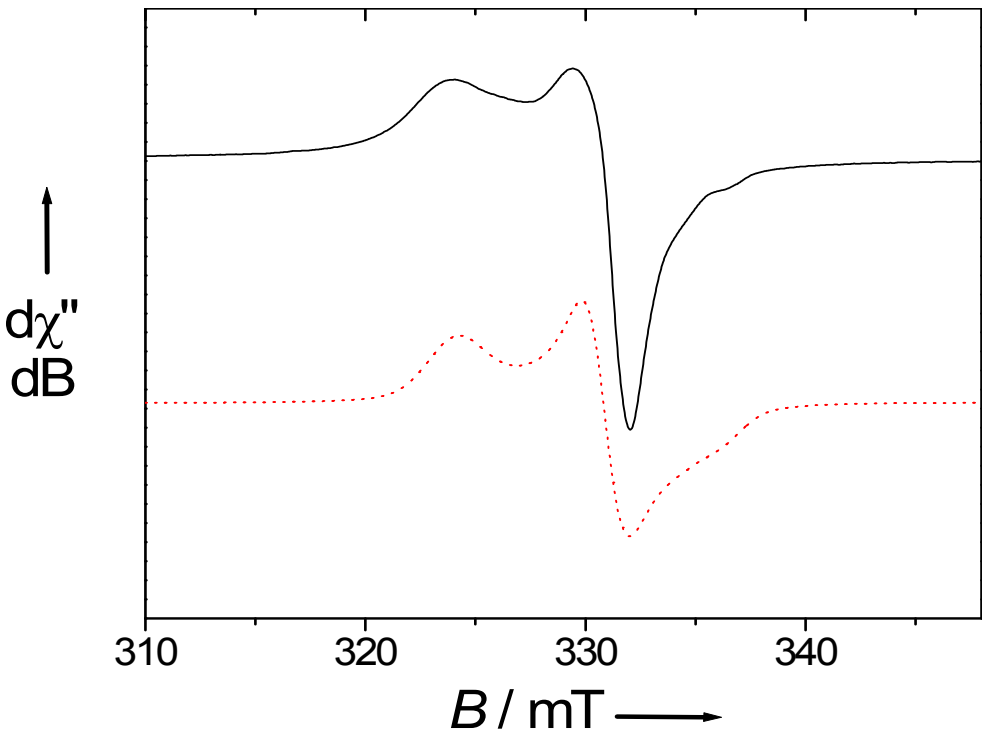

Figure S15. EPR spectrum of a 1 mM CH_2Cl_2 solution of the electrochemically generated $\mathbf{3}^{+}$. Solid lines: experimental spectra, dotted red lines: simulation using parameters given in Table 2. Microwave freq. 9.34 GHz, power = 5 mW, mod. freq. 100 KHz, amp. 0.3 mT, T = 100 K.

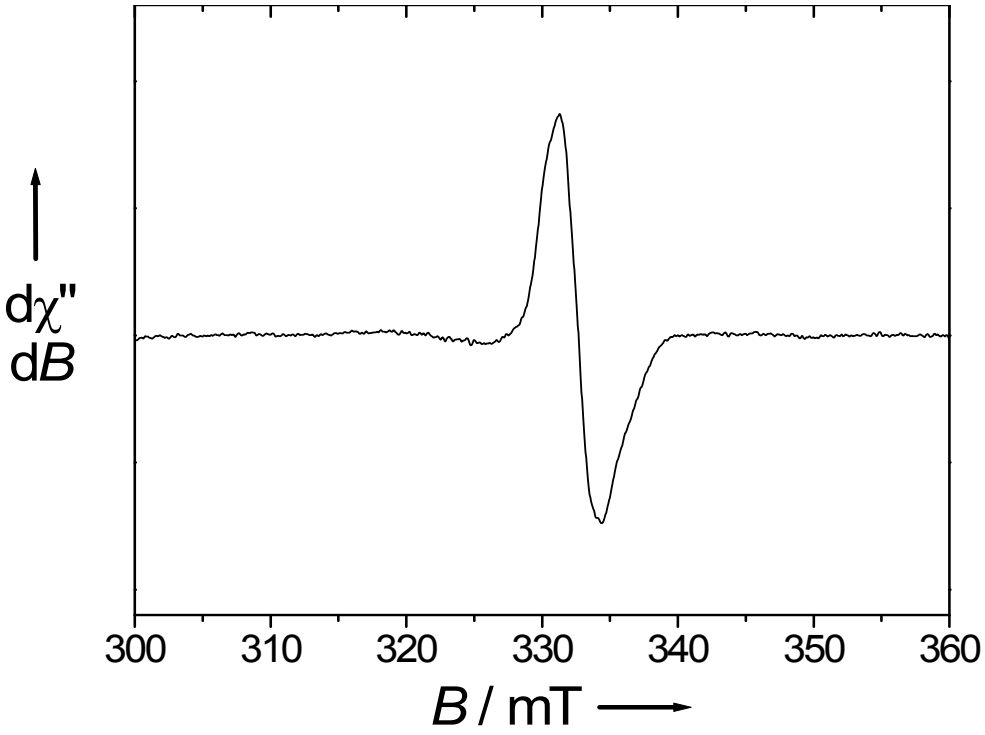

Figure S16. EPR spectrum of a 4 mM THF solution of **3**$^{-}$ (chemically prepared by reduction of **3** with NaHg amalgam). Microwave freq. 9.33 GHz, power = 5 mW, mod. freq. 100 KHz, amp. 0.3 mT, T =100 K.

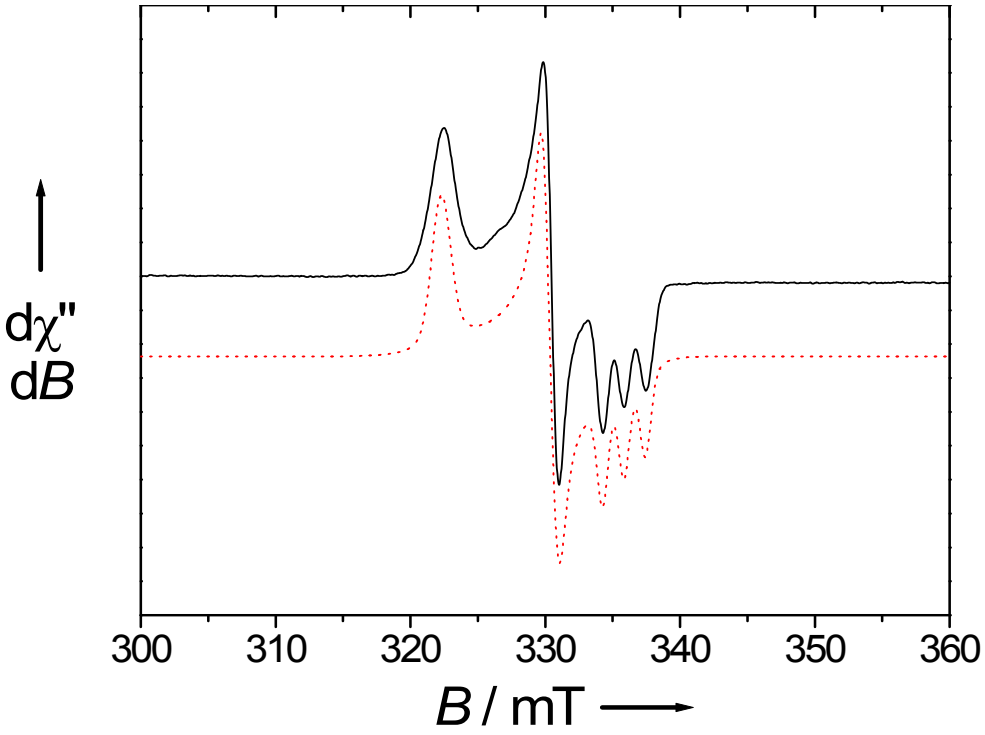

Figure S17. EPR spectrum of a 4 mM THF solution of **3**$^{-}$ (chemically prepared by reduction of **3** with NaHg amalgam) after exposure for 2 minutes to air. Solid lines: experimental spectra, dotted red lines: simulation using parameters given in Table 2. Microwave freq. 9.33 GHz, power = 5 mW, mod. freq. 100 KHz, amp. 0.1 mT, T = 100 K.

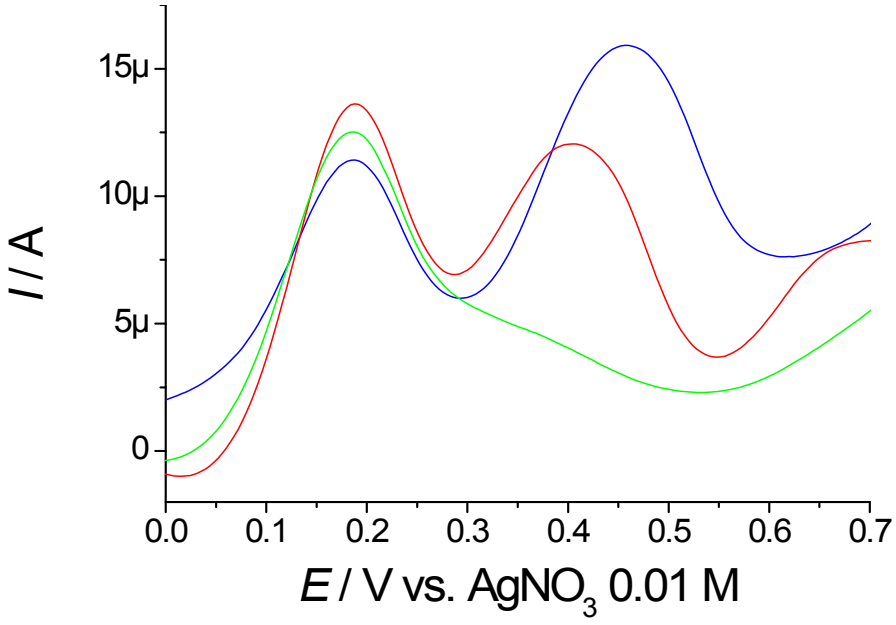

Figure S18. Differential Pulse Voltammetry curves of 1 mM CH_2Cl_2 (+0.1 M TBAP) solutions of the complexes: (green) ferrocene, (blue) **2** + ferrocene, (red) **3** + ferrocene. The potentials are quoted relative to the 0.01 M $AgNO_3$ reference electrode, which was used in the experiment. T = 298 K.

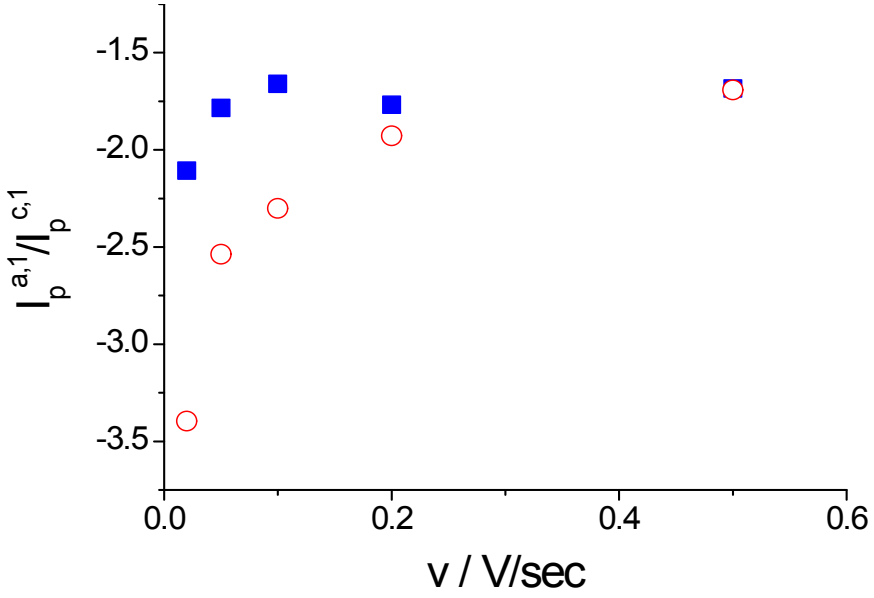

Figure S19. Evolution of the reversibility of the oxidation wave as a function of the scan rate for 1 mM CH_2Cl_2 (+0.1 M TBAP) solutions of the complexes: (blue squares) **2**, (red circles) **3**. T = 298 K.

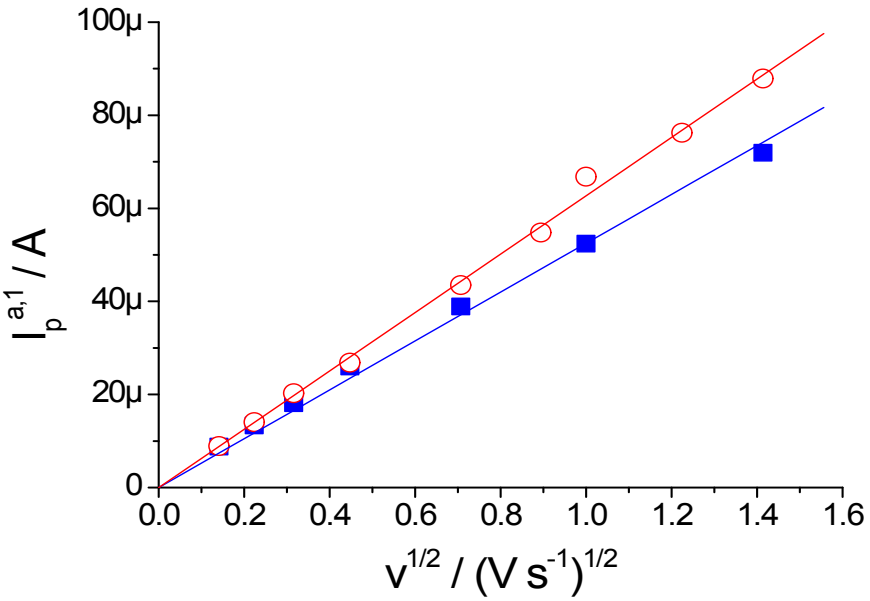

Figure S20. Plot of $I_p^{a,1}$ as a function of the square root of the scan rate, showing that the oxidation process is controlled by the diffusion. Conditions are 1 mM CH_2Cl_2 (+0.1 M TBAP) solutions of the complexes at T = 298 K: (blue squares) **2**, (red circles) **3**.